Supplementary Information

Solution-Processed Ferroelectric Terpolymer Nanocomposites with High Breakdown Strength and Energy Density Utilizing Boron Nitride Nanosheets

Qi Li,[1] Guangzu Zhang,[1,2] Feihua Liu,[3] Kuo Han,[1] Matthew R. Gadinski,[1] Chuanxi Xiong[3] and Qing Wang[1]

[1] Department of Materials Science and Engineering, The Pennsylvania State University, University Park, Pennsylvania 16802, USA.

[2] School of Optical and Electronic Information, Huazhong University of Science and Technology, Wuhan, Hubei 430074, P. R. China

[3] Key Laboratory of Advanced Technology for Materials Synthesis and Processing, and School of Materials Science and Engineering, Wuhan University of Technology, Wuhan 430070, P. R. China.

Experimental details

Thermal conductivity measurement: To measure thermal conductivity, rectangular strip shaped specimens were microtomed from the blanket films. These 250 micron wide and 1.5 mm long specimens were then mounted as freestanding beams in a custom designed jig with both ends clamped. One end of the specimen was heated with a resistance temperature detector (RTD) heater. The other clamping end acts as a heat sink, thereby maintaining a temperature gradient in the specimen. An Infrascope II thermal microscope (Quantum Focus Instruments Corporation) is used to spatially map the temperature of the specimen. The liquid nitrogen-cooled Indium-Antimonide infrared focal plane array detector in the microscope head measures the radiance from target objects to calculate the temperature. The spatial and temperature resolutions of this infrared microscope are 3 microns and 0.1 °C respectively. The temperature profile along the specimen length, obtained from the IR microscope, is used to calculate the thermal conductivity of the specimen.

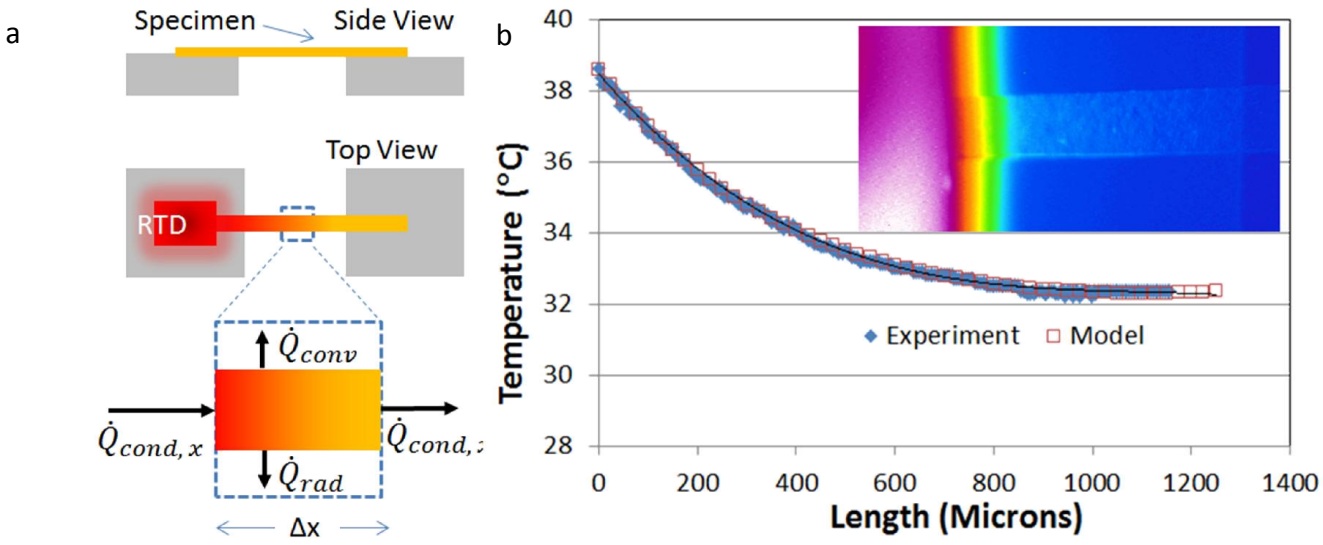

Scheme S1. (**a**) Schematic diagram showing the experimental setup and a control volume in the specimen for energy balance, (**b**) measured spatial temperature gradient (infrared image shown inset) is compared with model to extract thermal conductivity.

Mathematical model for thermal conductivity measurement of the specimen can be found from the heat transfer model of a simple rectangular fin [1]. The energy conservation principle is applied to a specimen element of length Δx and width w. Heat enter and leaves the element by conduction and is lost through both convection and radiation. For a surface area of S and cross sectional area A, heat incoming to the control volume by conduction is balanced by heat leaving in the form of conduction, convection and radiation. This is schematically shown in Scheme S1(A) and can be expressed as,

$$-KA\frac{dT}{dx}\Big|_x + KA\frac{dT}{dx}\Big|_{x+\Delta x} - hS(T - T_\infty) - \varepsilon\sigma S\left(T^4 - {T_\infty}^4\right) = 0 \quad (1)$$

Here, K is the thermal conductivity of the specimen, T_∞ is the ambient temperature, h is convection heat transfer coefficient, ε is emissivity and σ is Stefan – Boltzmann constant. For small temperature differences, equation (1) can be approximated as,

$$-KA\frac{dT}{dx}\Big|_x + KA\frac{dT}{dx}\Big|_{x+\Delta x} - \left(h + \varepsilon\sigma 4{T_\infty}^3\right)S(T - T_\infty) = 0 \quad (2)$$

This equation can be rewritten as,

$$KA\frac{d^2T}{dx^2}\Delta x - \left(h + \varepsilon\sigma 4{T_\infty}^3\right)P\Delta x(T - T_\infty) = 0 \quad (3)$$

Here, P is the perimeter of the specimen cross-section. Equation 3 can be further rearranged as,

$$\frac{d^2\theta}{dx^2} - m^2\theta = 0 \quad (4)$$

where, $m^2 = \left(h + \varepsilon\sigma 4{T_\infty}^3\right)\frac{P}{KA}$ and $\theta = (T - T_\infty)$

Solution of this second order differential equation can be given by

$$T(x) - T_\infty = C_1 \sinh(mx) + C_2 \cosh(mx) \quad (5)$$

The integration constants C_1 and C_2 can be found from boundary conditions, $T|_{x=0} = T_w$ and $\frac{dT}{dx}\Big|_{x=L} = 0$ (Newtonian cooling for small area). By defining sample length such that

$dT/dx = 0\ at\ x = L$ (no heat input by heat conduction) and solving for the boundary conditions, we get $C_2 = (T_w - T_\infty)$ and $C_1 = -C_2 \tanh(mL)$. Substituting constants in equation 5 and rearranging gives the temperature distribution as,

$$T(x) = T_\infty + (T_w - T_\infty)\frac{\cosh(m(L-x))}{\cosh(mL)}, \text{ where } \quad m = \left[\left(h + \varepsilon\sigma 4{T_\infty}^3\right)\frac{P}{KA}\right]^{1/2} \tag{6}$$

Next, using the infra-red thermal microscope data, the spatial temperature profile *T(x)* and the hot end temperature T_w can be accurately measured as shown by the representative temperature profile in Scheme S1(B). Equation 6 therefore facilitates us to plot the modeled *T(x)* as function of thermal conductivity with the measured *T(x)*. However, to obtain the modeled *T(x),* accurate measurement of natural convective heat transfer coefficient is required. This can be accomplished easily from the measurement of temperature distribution of air around a heated surface [2]. Here, the temperature distribution in the thermal boundary layer is given by

$$\ln\frac{T-T_\infty}{T_w-T_\infty} = sx \tag{7}$$

where, *s* is a constant determined from the plot of logarithm of temperature difference ratio against distance (*x*) from the specimen surface at temperature T_w. Then local natural convective heat transfer coefficient of air can found from the product of thermal conductivity of air, k_{air} and *s* [3].

$$h = k_{air}s \tag{8}$$

The technique was calibrated with silicon oxide specimens, whose thermal conductivity is of similar magnitude as the polymer composite specimens studied in this work [2]. The measured thermal conductivity for oxide was found to be 1.2 W/m-K which is a very good match with previously reported values in the literature [4-6].

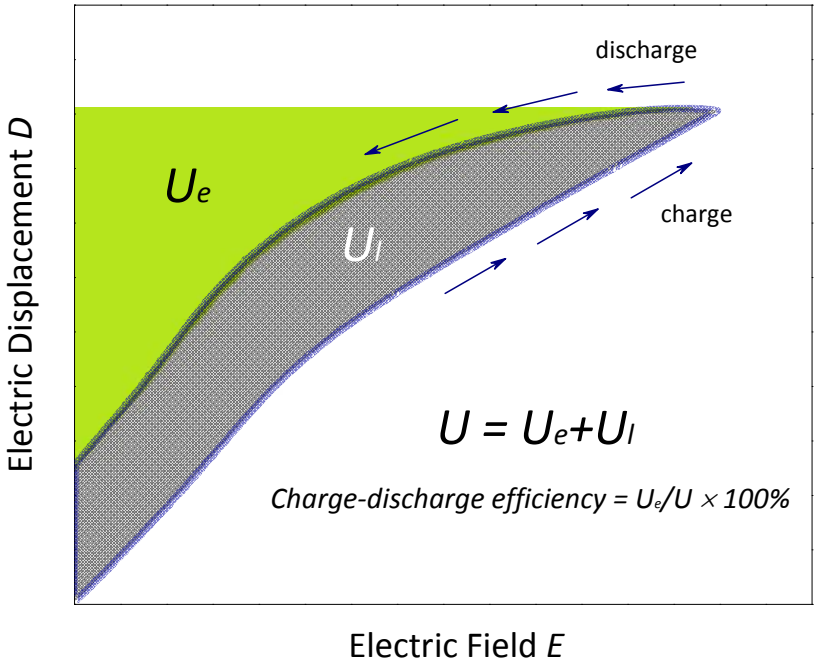

Figure S1. Schematic *D*-*E* loop for a dielectric material. The discharged energy density (U_e) is represented by the green area between the discharge curve and the electric displacement axis, while the energy dissipated (U_l) is indicated by the grey area surrounded by the loop curve. Apparently, the totally charged energy density (U) equals to U_e plus U_l. The charge-discharge efficiency is defined as $U_e/U \times 100\%$.

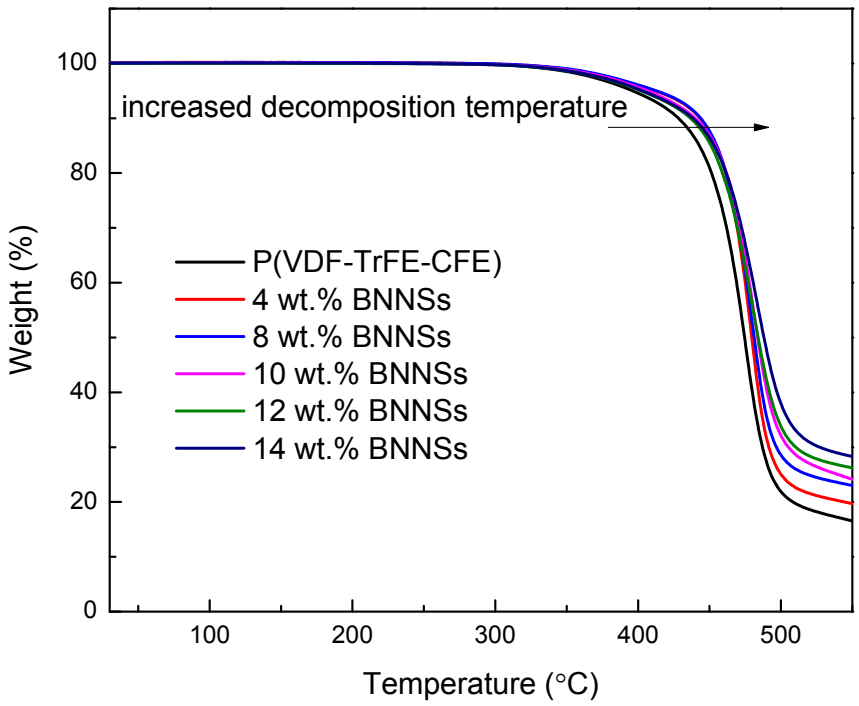

Figure S2. TGA curves of P(VDF-TrFE-CFE) and various P(VDF-TrFE-CFE)/BNNS nanocomposites. The decomposition temperature of the terpolymer is shift to higher temperature upon the incorporation of BNNSs, indicating the thermal stability of the host polymer is improved by the nanofillers

Table S1. Comparison of the filler content between the pre-determined and calculated values .

Pre-determined loading of BNNSs (wt.%)	4	8	10	12	14
Calculated loading of BNNSs (wt.%) [a)]	4.0	8.2	9.9	12.1	14.2

a) Calculation is based on the TGA data

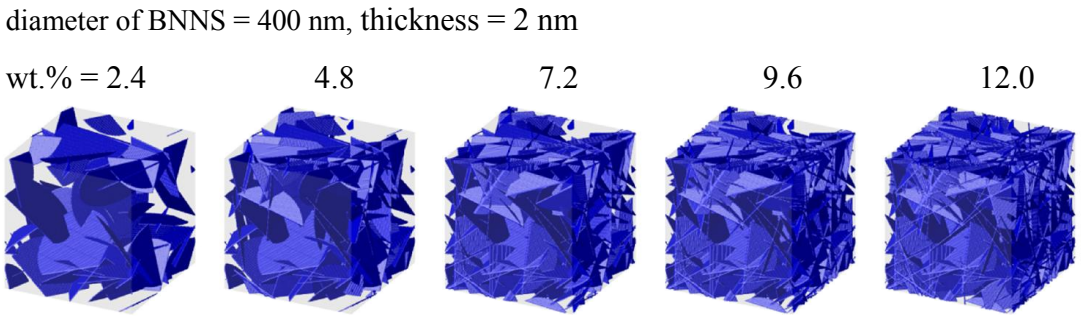

Figure S3. Simulated microstructure of P(VDF-TrFE-CFE)/BNNS nanocomposites with different filler contents

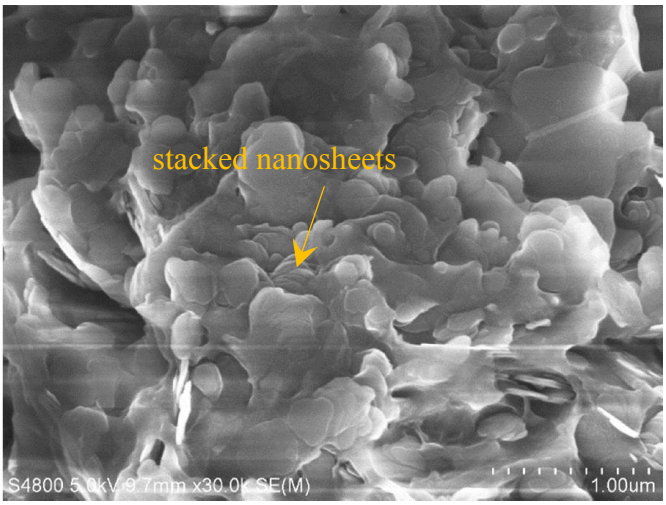

Figure S4. Cross-section SEM image of P(VDF-TrFE-CFE)/BNNS nanocomposite with 14 wt.% of BNNSs

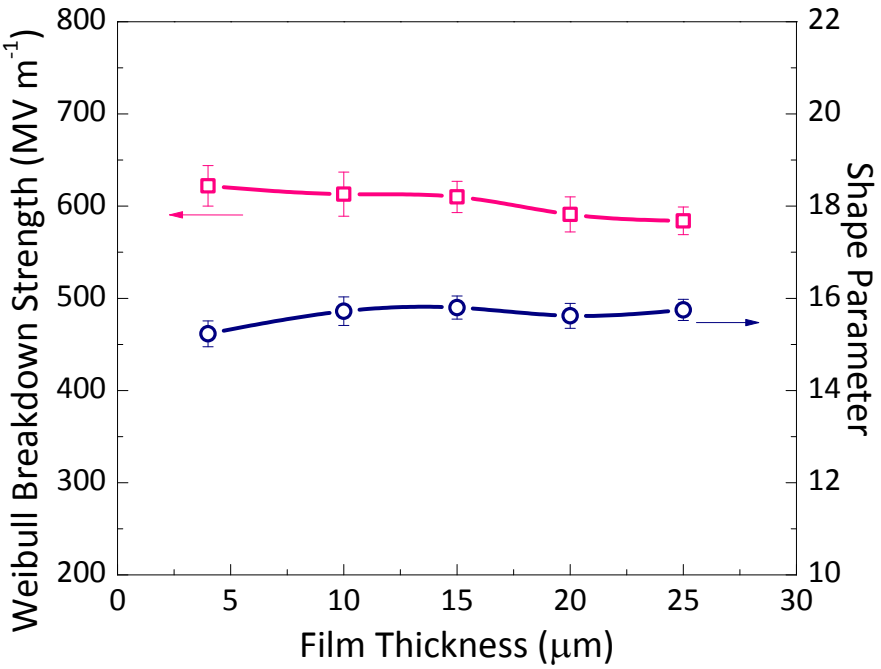

Figure S5. Weibull breakdown strength and shape parameter as functions of film thickness

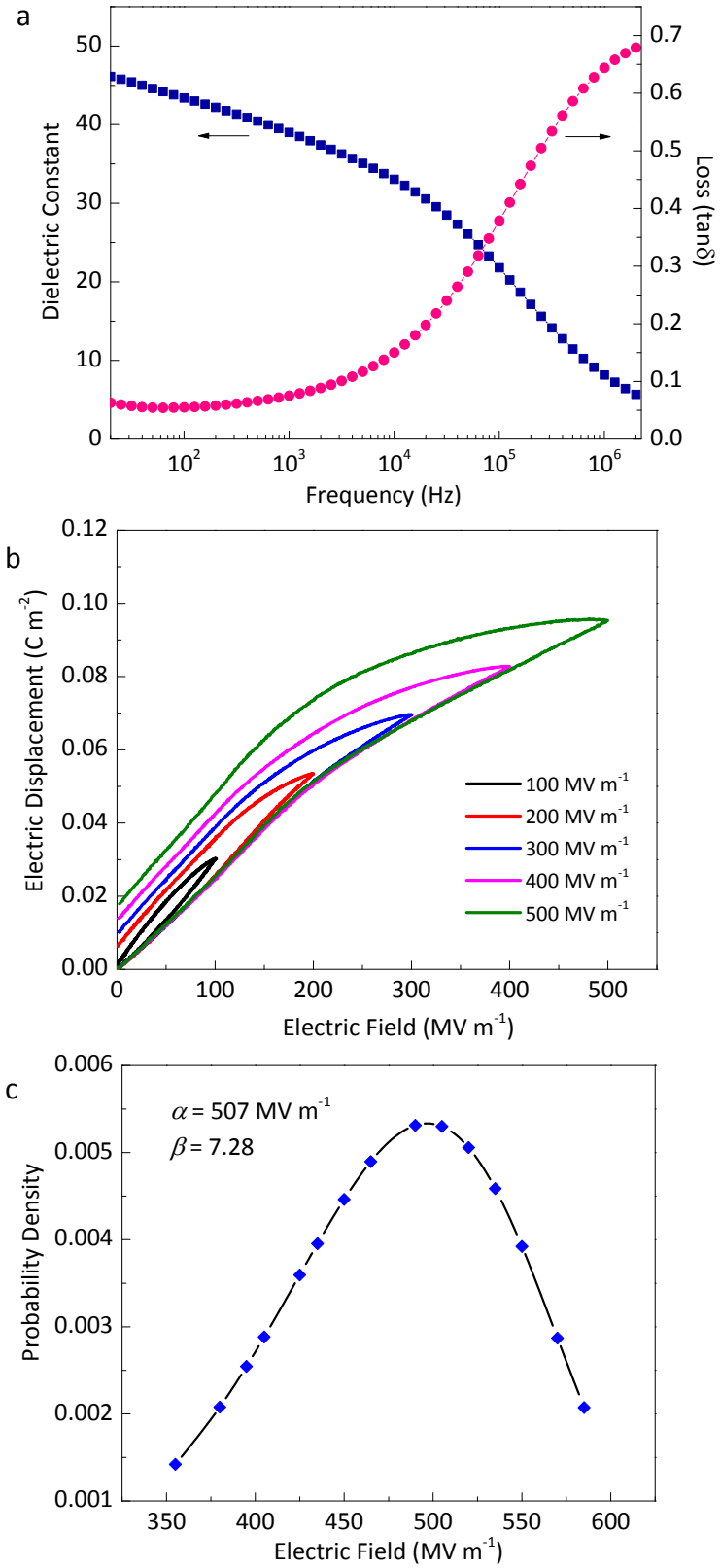

Figure S6. (**a**) Frequency dependent dielectric constant and loss, (**b**) *D-E* loops at varied electric fields and (**c**) Weibull plots of melt-stretched P(VDF-TrFE-CFE).

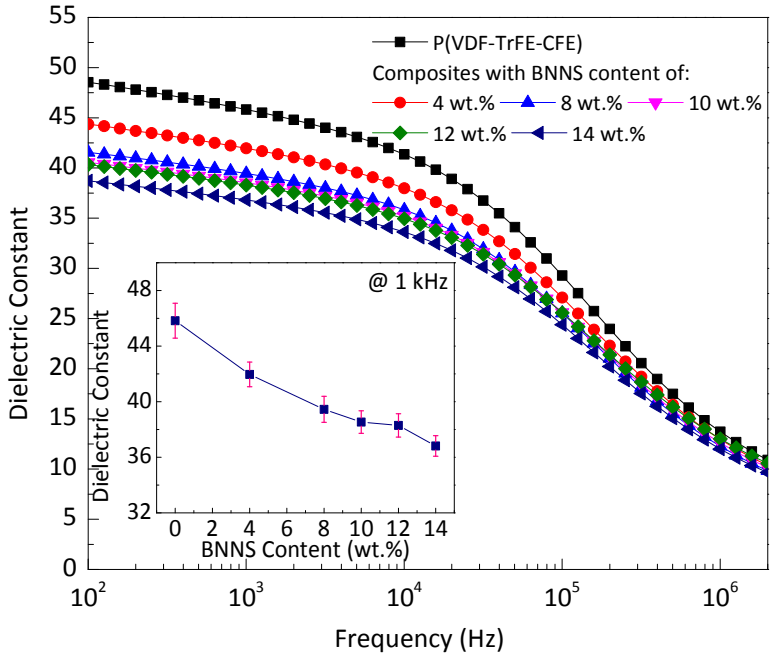

Figure S7. Frequency dependence of dielectric constant of P(VDF-TrFE-CFE)/BNNS nanocomposites with different contents of BNNSs. Inset: Dielectric constant of P(VDF-TrFE-CFE)/BNNS nanocomposites at 1 kHz as a function of filler content.

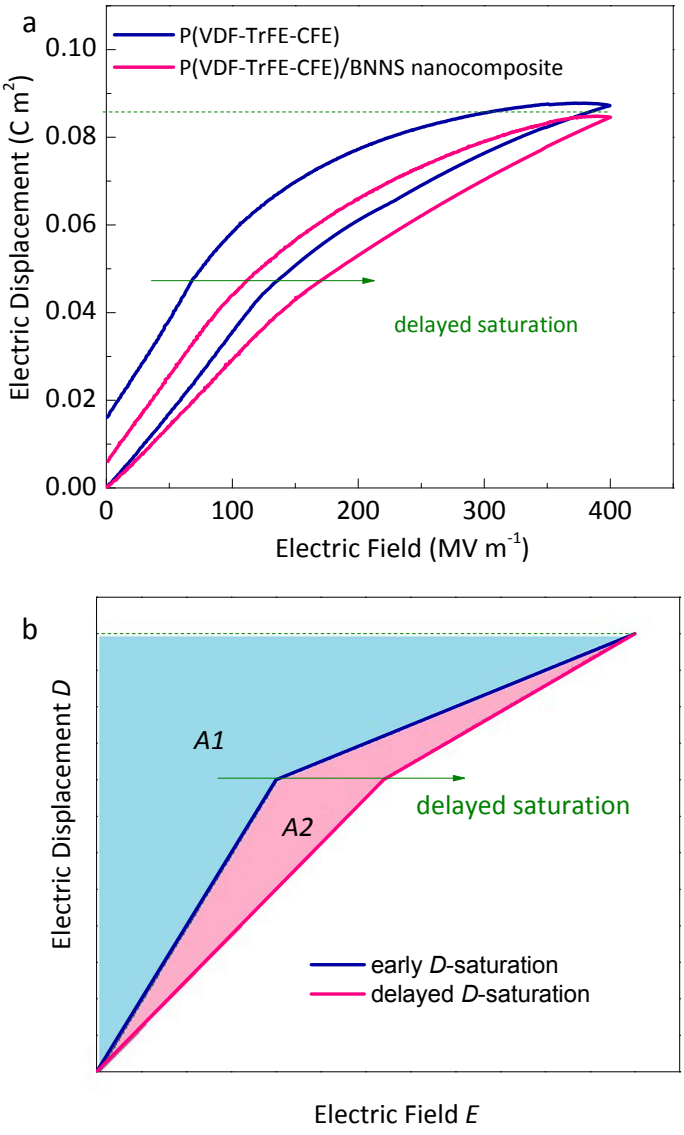

Figure S8. (**a**) *D*-*E* loops of pristine P(VDF-TrFE-CFE) and P(VDF-TrFE-CFE)/BNNS nanocomposite with 12 wt.% of BNNSs at an electric field of 400 MV m^{-1}, (**b**) schematic *D*-*E* loops showing the early and delayed *D*-saturation fashions. While the blue area (*A1*) represents the energy density of the dielectric with early *D*-saturation, the red area (*A2*) indicates the superior part of the energy density from delayed *D*-saturation.

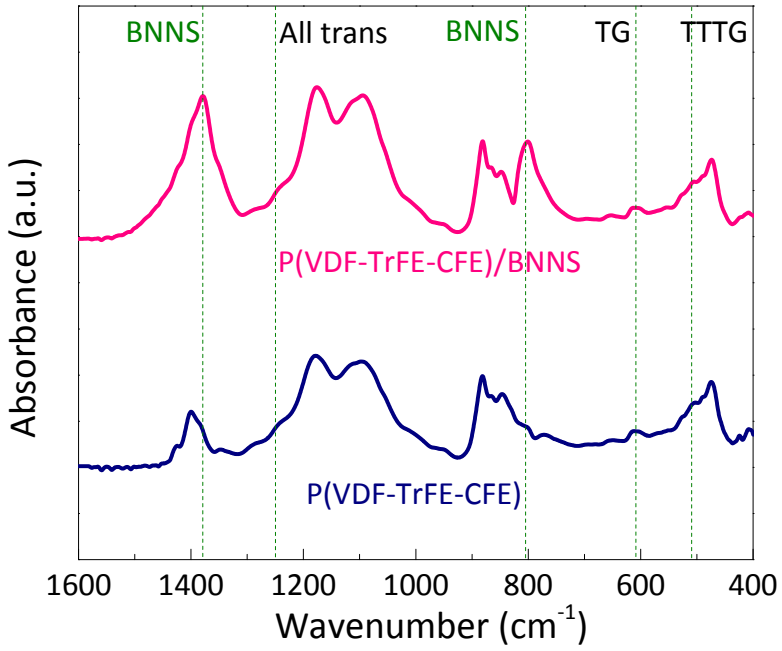

Figure S9. ATR-FTIR spectra of pristine P(VDF-TrFE-CFE) and P(VDF-TrFE-CFE)/BNNS nanocomposite with 12 wt.% of BNNSs. The three characteristic peaks located at 509, 610 and 1249 cm^{-1} correspond to the T_3G, TG and long *trans* sequence conformations, respectively. The fraction of each chain conformation (F_i) is analyzed quantitatively following the equation: $F_i = A_i/(A_1+A_2+A_3)$, where i = 1, 2, 3, and A_1, A_2, A_3 are the absorbencies of the T_3G, TG and long *trans* sequence conformations, respectively. The calculations show that the F_1, F_2 and F_3 values are 44%, 25% and 31% for pristine terpolymer and 42%, 26% and 32% for the nanocomposite, suggesting the crystalline phases almost remain unaffected upon blending with BNNSs.

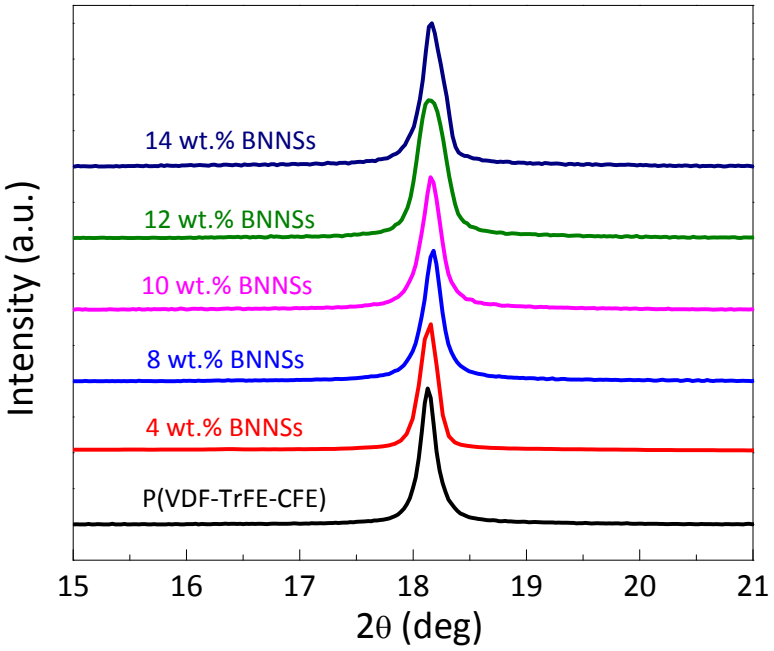

Figure S10. XRD patterns of pristine P(VDF-TrFE-CFE) and a series of P(VDF-TrFE-CFE)/BNNS nanocomposites with different filler contents.

Table S2. Crystallization temperature, crystallinity and mean size of the crystalline domain of P(VDF-TrFE-CFE) and P(VDF-TrFE-CFE)/BNNS nanocomposites with various contents of BNNSs. The mean sizes of the crystalline domains are calculated on the basis of the Scherrer equation described as $D_{hkl} = (K \cdot \lambda)/(\beta_{hkl} \cdot \cos\theta)$, where D_{hkl} is the mean crystallite size along the [hkl] direction, K is a dimensionless shape factor, λ is the X-ray wavelength, β_{hkl} is the line broadening at half the maximum intensity for the (hkl) diffraction, and θ is the Bragg angle.

Sample	T_c [°C][a)]	Crystallinity [%][a)]	D [nm][b)]
P(VDF-TrFE-CFE)	104	31.4	49.4
P(VDF-TrFE-CFE) with 4 wt.% BNNSs	108	32.9	44.3
P(VDF-TrFE-CFE) with 8 wt.% BNNSs	109	34.5	42.0
P(VDF-TrFE-CFE) with 10 wt.% BNNSs	110	34.7	36.1
P(VDF-TrFE-CFE) with 12 wt.% BNNSs	110	35.0	29.0
P(VDF-TrFE-CFE) with 14 wt.% BNNSs	109	33.4	34.9

[a)] Determined by DSC; [b)] Determined by XRD.

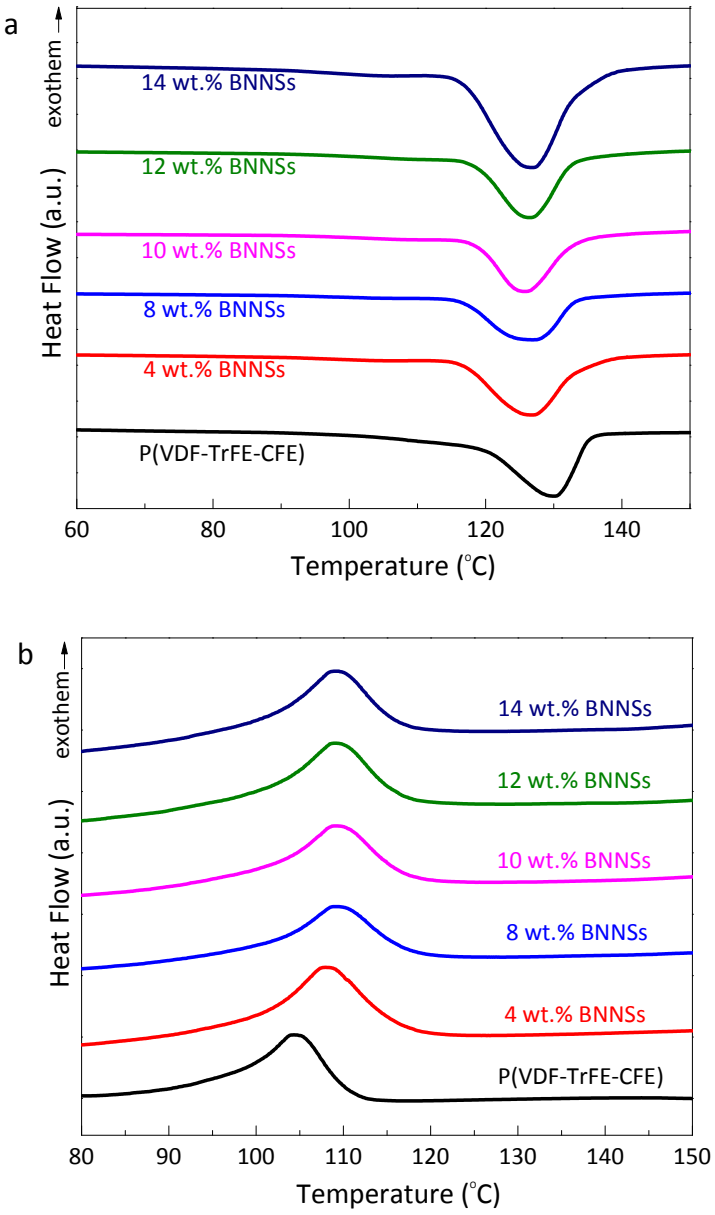

Figure S11. DSC curves of P(VDF-TrFE-CFE) and P(VDF-TrFE-CFE)/BNNS nanocomposites during the (**a**) heating and (**b**) cooling cycle.

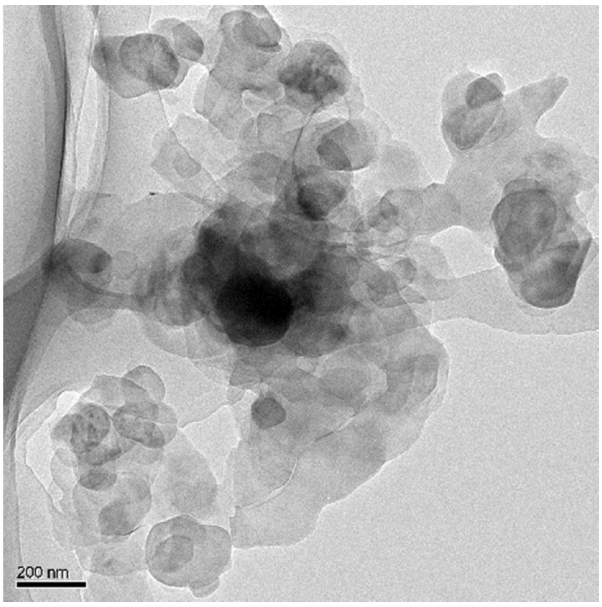

Figure S12. Typical TEM image of sl-BNNSs.

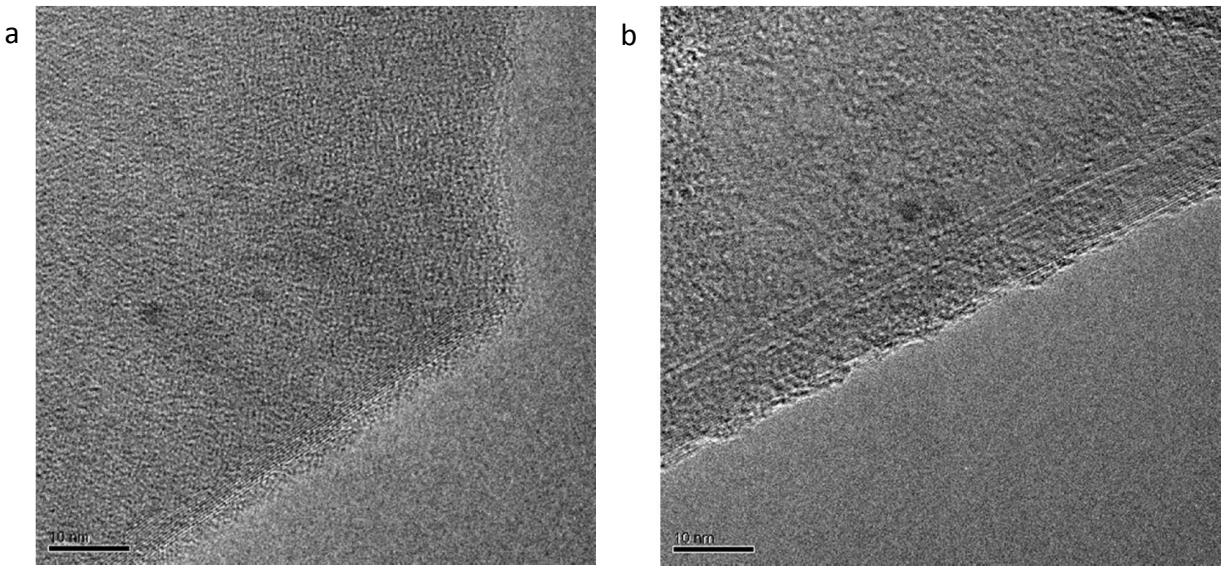

Figure S13. Typical TEM images of (a) 8t-BNNS and (b) 15t BNNS. Scale bar, 10 nm.

Supplementary Information References

[1] F.P. Incropera, D.P. DeWitt, Fundamentals of heat and mass transfer, John Wiley & Sons, New York, 2007.

[2] M.T. Alam, A.P. Raghu, M.A. Haque, C. Muratore, A.A. Voevodin, International Journal of Thermal Sciences, 73, 1-7 (2013).

[3] C. Roldán, M. Buendía, R. Cibrián, R. Salvador, E. Ramón, J.V. Herráez, R. Belda, M. Dolz, European Journal of Physics, 14, 128 (1993).

[4] T. Yamane, N. Nagai, S.-i. Katayama, M. Todoki, Journal of Applied Physics, 91, 9772-9776 (2002).

[5] O.W. Kading, H. Skurk, K.E. Goodson, Applied Physics Letters, 65, 1629-1631 (1994).

[6] S. Callard, G. Tallarida, A. Borghesi, L. Zanotti, Journal of Non-Crystalline Solids, 245, 203-209 (1999).